The geometry of the ICRF-induced wave–SOL interaction. A multi-machine experimental review in view of the ITER operation

L. Colas, G. Urbanczyk, M. Goniche, J. Hillairet, J.-M. Bernard, C. Bourdelle, N. Fedorczak, C. Guillemaut, W. Helou, V. Bobkov, et al.

IOP Publishing | International Atomic Energy Agency Nuclear Fusion

Nucl. Fusion **62** (2022) 016014 (17pp) https://doi.org/10.1088/1741-4326/ac35f9

The geometry of the ICRF-induced wave–SOL interaction. A multi-machine experimental review in view of the ITER operation

L. Colas[1,*], G. Urbanczyk[1,2], M. Goniche[1], J. Hillairet[1], J.-M. Bernard[1], C. Bourdelle[1], N. Fedorczak[1], C. Guillemaut[1], W. Helou[3], V. Bobkov[4], R. Ochoukov[4], Ph. Jacquet[5], E. Lerche[5,6], X. Zhang[7], C. Qin[7], C.C. Klepper[8], C. Lau[8], B. Van Compernolle[9], S.J. Wukitch[10], Y. Lin[10], M. Ono[11], JET Contributors[a], the ASDEX Upgrade Team[b], the EAST Team[c], the WEST Team and ITPA IOS

[1] CEA, IRFM, F-13108 St-Paul-Lez-Durance, France
[2] Key Laboratory of Optoelectronic Devices and Systems, College of Physics and Optoelectronic Engineering, Shenzhen University, Shenzhen 518060, China
[3] ITER Organization, Route de Vinon-sur-Verdon, CS 90 046, 13067 St. Paul Lez Durance Cedex, France
[4] Max-Planck-Institut für Plasmaphysik, Boltzmannstraße 2, 85748 Garching, Germany
[5] CCFE, Culham Science Centre, Abingdon, Oxfordshire OX14 3DB, United Kingdom
[6] Laboratory for Plasma Physics, Royal Military Academy, 1000 Brussels, Belgium
[7] Institute of Plasma Physics, CAS, Hefei, Anhui 230031, China
[8] Oak Ridge National Laboratory, 1 Bethel Valley Rd, Oak Ridge, TN 37830, United States of America
[9] General Atomics, San Diego, CA, United States of America
[10] Plasma Science Fusion Center, MIT, Cambridge, MA 02139, United States of America
[11] Princeton Plasma Physics Laboratory, Princeton, NJ 08543, United States of America

E-mail: laurent.colas@cea.fr

Received 31 May 2021, revised 2 August 2021
Accepted for publication 3 November 2021
Published 13 December 2021

Abstract

As part of ITPA-Integrated Operational Scenario activities, this contribution reviews recent experimental characterizations of radio-frequency (RF)-induced scrape-off layer (SOL) modifications of various tokamaks worldwide and of the LArge Plasma Device at UCLA. The phenomenology, as observed using a large variety of measurement techniques, is consistent with expectations from RF sheath rectification. Emphasis is then put on the complex three-dimensional (3D) spatial patterns of the RF–SOL interaction, in relation to the magnetic topology and the spatial distribution of RF currents over the metallic structures surrounding the RF wave launchers. Dependence on the local plasma parameters in the antenna vicinity is also briefly addressed. The final part discusses implications for future devices.

* Author to whom any correspondence should be addressed.
[a] See Joffrin *et al* 2019 (https://doi.org/10.1088/1741-4326/ab2276) for the JET Contributors.
[b] See Meyer *et al* 2019 (https://doi.org/10.1088/1741-4326/ab18b8) for the ASDEX Upgrade Team.
[c] See Ida *et al* 2018 (https://doi.org/10.1088/1361-6587/aa9b03) for the EAST Team.

Keywords: RF sheath, ICRH, biasing, $E \times B$ convection, erosion, heat load

(Some figures may appear in colour only in the online journal)

1. Introduction

Of the three additional heating methods envisaged for ITER, waves in the ion cyclotron range of frequencies (ICRF, 30–100 MHz in present devices) are attractive as the only one capable of direct ion heating and central power deposition at high densities. Yet, since the first use of ICRF waves with scrape-off layer (SOL) plasma in magnetic fusion devices, this non-linear interaction has attracted attention. This interaction is now generally attributed to radio-frequency (RF) sheath rectification. In view of ITER, the topic has gained renewed interest. ICRF was applied in metallic machines where RF-enhanced wall sputtering might increase core plasma contamination with high-Z impurities. Even when not critical on short pulses, such spurious processes could hinder the machine lifetime if their effects cumulate over long periods. A further challenge is to combine ICRH with other subsystems in Integrated Operational Scenarios (IOS). ICRF-induced SOL modifications might perturb the operation of the other actuators, e.g. lower hybrid (LH) wave coupling and hot spots in present devices. A recent multi-machine task in view of ITER was to ease ICRF coupling by localized gas injection, while disturbing the plasma core as little as possible [1]. Within ITPA-IOS, this new contribution reviews the experimental characterization of ICRF-induced SOL modifications over the past 20 years of various tokamaks worldwide and on the LArge Plasma Device (LAPD). Reference [2] reviewed earlier experiments.

ICRF waves are meant to heat either the main ion species of the plasma discharge at the harmonics of their cyclotron frequency or a minority species at its main cyclotron frequency. Minority ions are introduced on purpose in typical concentrations of a few percent. Energetic ions from neutral beam injection (NBI) or intrinsic light impurities can also play this role. In future devices, ICRF waves may also be used for current drive via a combination of electron Landau damping and transit-time magnetic pumping. In general, the scenarios are devised so that the resonant wave/particle interactions occur near the plasma centre. Once accelerated, the resonant species re-distributes the power gained from the waves to the other plasma constituents via collisions. Unless explicitly mentioned, the reported results were obtained with the D[H] minority heating scheme. The main exceptions are the NSTX spherical tokamak and the LAPD linear device, both using high-harmonic fast wave (FW) heating of D^+ and He^{2+} plasmas respectively. Although these are the workhorse scenarios of present devices, they are not the main heating schemes intended for future DT machines. It is believed that by their nature, the SOL processes described below are qualitatively generic. However the ICRF-induced SOL modifications might vary in amplitude with the ICRF wave coupling properties or the single pass power absorption through the plasma core, which are scenario-dependant. The mass of the main ions, together with the presence light impurities, are also known to affect the sputtering of wall materials. The paper will discuss our present knowledge on these aspects and the uncertainties for extrapolating quantitatively to DT machines.

While the magnitude of adverse effects should be minimized, we also emphasize the 3D spatial distribution of the SOL modifications. Figure 1 sketches the typical structure of present ICRF wave launchers. They consist of phased arrays of current straps housed in individual metallic boxes electrically grounded to the machine vessel. The straps are generally oriented along the poloidal direction of the tokamak, but may be tilted perpendicular to the local confining magnetic field. The number of straps is variable. Each is fed by an independent coaxial transmission line. However, the straps may be grouped to reduce the number of feeding lines and/or improve the load resilience. Antenna boxes are generally partially closed on their plasma side by a Faraday screen, a tight array of metallic rods ideally parallel to the confinement magnetic field. Antenna boxes are generally surrounded by private limiters. The active straps induce RF currents on all neighbouring passive metallic structures. Understanding the RF sheath complex 3D patterns, in relation with the plasma magnetic topology and the spatial distribution of all these RF currents, provides hints for judicious port allocation, antenna design and operation. This clarifies which plasma-facing components (PFCs) are more likely to be eroded, and which species are sputtered in mixed-materials walls like ITER. Reproducing the measured patterns also puts strong constraints on interpretative RF sheath models. Reference [3] proposes a recent tutorial on RF sheath modelling in magnetic fusion plasmas. References [4–6] reviewed some comparisons of experiments with modelling in realistic geometry.

The paper is organized as follows. Section 2 describes the physical nature of ICRF-induced SOL modifications, stressing its consistency with expectations for RF sheath rectification. We also briefly present other physical processes that might affect the SOL, as well as specific techniques used to measure key SOL quantities averaged over thousands of RF periods. Section 3 outlines the complex 3D spatial structure of these SOL modifications. We separate regions connected ('near field') and not connected magnetically to the active ICRF wave launchers ('far field'). Sections 4 and 5 discuss respectively the roles of the antenna design and electrical setup, and then of the local plasma parameters, in the 'near-field' SOL modifications. Section 6 attempts some extrapolation of the present results to future long pulse metallic DT

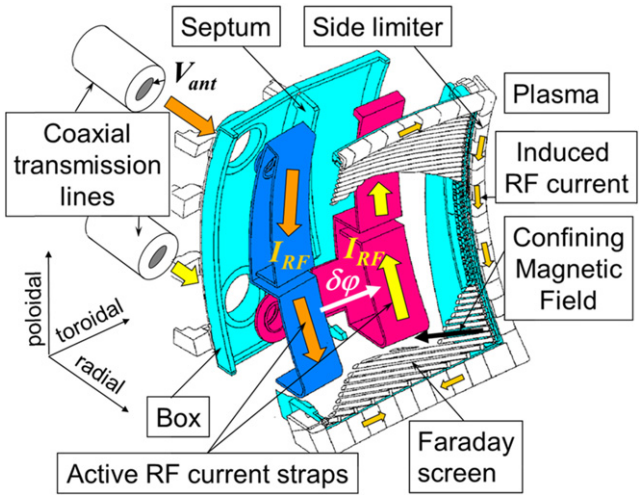

Figure 1. Sketch of a typical present-day ICRF wave launcher, showing its main components. Schematic definition of antenna RF voltage V_{ant} and phasing $\delta\varphi$ between adjacent strap RF currents.

machines, and outlines some remaining uncertainty in this prospect.

2. Nature of ICRF-induced SOL modifications, specific measurement techniques

2.1. RF sheath rectification basics

The SOL of magnetized plasma devices is a region where open magnetic field lines intercept material boundaries. The plasma is not confined along the field lines, whose extremities are therefore subject to large particle and heat fluxes. At any plasma–material interface, sheaths spontaneously build-up as thin boundary layers, of typical sizes 1-100micron in current fusion devices, in order to equilibrate the ion and electron fluxes onto the wall, thus preserving the electro-neutrality of the bulk plasma far from the wall. This equilibration is governed by a I–V electrical characteristic linking the current density I on the wall to the voltage drop V across the sheath. The textbook I–V characteristic is written

$$I = I_{\rm sat}\left[1 - \exp\left(-\frac{e\,(V - V_{\rm f0})}{kT_{\rm e}}\right)\right], \qquad (1)$$

where $I_{\rm sat}$ is the ion saturation current, $T_{\rm e}$ is the local electron temperature and $V_{\rm f0}$ is the floating potential in the absence of ICRF. On the right-hand side, the two terms correspond respectively to the collected ion and electron currents. While ordinary sheaths are static, intense RF electric fields in the vicinity of the wall may induce strong RF oscillations $V_{\rm RF}$ of the sheath voltage at the wave frequency. Since the sheath electrical properties (e.g. I–V characteristic (1)) are non-linear, $V_{\rm RF}$ tends to shift the time-averaged (direct current (DC)) $I_{\rm DC}$–$V_{\rm DC}$ characteristic of the sheath with respect to its thermal expression (1). The modified characteristic takes the general form

$$I_{\rm DC} = I_{\rm sat}\left[1 - \exp\left(-\frac{e\,(V_{\rm DC} - V_{\rm b}\,(V_{\rm RF}) - V_{\rm f0})}{kT_{\rm e}}\right)\right]. \qquad (2)$$

Rectification thus acts as if the local wall elements (generally grounded in tokamaks) were electrically biased to the DC potential $V_{\rm b}$. Several expressions for $V_{\rm b}$ have been proposed in the literature. For example, one can obtain a quasi-static limit by inserting $V(t) = V_{\rm DC} + V_{\rm RF}\cos(\omega_0 t)$ into (1) and then averaging $I(t)$ over time [7]:

$$\frac{eV_{\rm b}\,(V_{\rm RF})}{kT_{\rm e}} = \ln\left[I_0\left(\frac{e\,|V_{\rm RF}|}{kT_{\rm e}}\right)\right], \qquad (3)$$

where $I_0\,(z) \equiv \frac{1}{\pi}\int_0^{\pi}\exp\left[z\,\cos\,(\varphi)\right]{\rm d}\varphi$ is the modified Bessel function of order 0. In all the proposed formulae, $V_{\rm b}$ scales as $|V_{\rm RF}|$ when $e|V_{\rm RF}| \gg kT_{\rm e}$. Most of the phenomenology described below is common with more familiar biasing experiments using electrodes, except that the DC bias is not controlled from outside but imposed by the RF waves. This 'self-biasing' is described in textbooks for non-magnetized sheaths in RF discharges [7, 8] but is more complicated in the presence of a static magnetic field tilted with respect to the wall [3]. In tokamaks, the sheath oscillations are hardly documented experimetally. Plasma diagnostics rather measure the DC bias and its consequences, averaged over many RF periods. On ASDEX Upgrade however, the antenna limiter tiles are equipped to measure the RF currents they collect [68]. In LAPD, reference [9] diagnosed the electrical RF and DC properties of RF-driven sheaths on a grounded plate magnetically connected to an ICRF antenna. The sheath RF impedance at the plate, defined as $V_{\rm RF}/I_{\rm RF}$ at the wave frequency, was measured as a function of the DC sheath voltage $V_{\rm DC}$ and compared to models.

2.2. SOL DC biasing due to RF sheath rectification

The SOL plasma is expected to react to the RF sheath rectification in a similar way as to an electrostatically biased electrode, by raising its local DC potential $V_{\rm DC}$ with respect to the (grounded) wall. If we request the sheath in equation (2) to float, the rectified $V_{\rm DC}$ becomes

$$V_{\rm DC} = V_{\rm f0} + V_{\rm b}(V_{\rm RF}). \qquad (4)$$

References [10–14] measured $V_{\rm DC}$ directly using emissive probes, while reference [15] estimated it from a retarding field analyzer (RFA) and reference [16] used triple Langmuir probes. Reference [13] also used ion sensitive probes suitable to measure $V_{\rm DC}$ at high SOL densities. The emissive and ion-sensitive probes were incorporated into a compound reciprocating diagnostic also measuring the local RF field amplitudes for different polarizations. References [12, 17–19] deduced changes of $V_{\rm DC}$ indirectly from the integration of DC radial electric fields. All techniques recorded $V_{\rm DC}$ in the range of several hundred volts near the Alcator C-mod antennas energized at megawatt levels. $V_{\rm DC}$ was also inferred from variations of the Langmuir probe floating potential $V_{\rm f}$, e.g. in [10, 20–27]. Interpreting the floating potentials might however be ambiguous: although $V_{\rm f}$ is related to DC plasma biasing, it is rather indicative of DC currents collected by the grounded probe (see paragraph 2.6).

2.3. Enhanced heat loads

DC SOL biasing is expected to increase the energy of the ions impinging the wall, thereby enhancing the plasma–wall interaction (PWI). References [15, 28] showed how ICRH locally modifies the ion parallel energy distribution on an RFA. Mean ion energies exceeding 150 eV were reported near the ASDEX Upgrade (AUG) two-strap antennas phased [0π] delivering 500 kW, while the ion temperature was 12.5 eV in the ohmic regime. Simulations in reference [15] suggest that, due to the sheath oscillations, the time-averaged energy distribution of the collected ions is not necessarily monotonic: it can exhibit two peaks if the wave frequency is lower than the local ion plasma frequency. Such distributions have been observed in capacitive plasma discharges [7] but are not documented in tokamak environment.

Heat loads onto the wall are locally increased during ICRH and were documented from surface temperature measurements using infrared (IR) cameras in JET [29–32], Tore Supra [33–36], NSTX [37] and WEST [27]. Reference [31] reported localized heat fluxes in the range of several MW m^{-2} normal to JET A2 antenna septa, depending on the RF voltage on the transmission lines, local density and RF feeding scheme. Reference [35] estimated up to 1 MW m^{-2} normal to Tore Supra Faraday screen bars. In actively cooled machines, quantitative information on heat fluxes is available from calorimetry. The principle is to compare inlet and outlet coolant temperatures for a given measured water flow in the pipes. Reference [36] concretely used calorimetry to compare the local sheath losses with two types of Faraday screens. A few percent of the energy launched by a Tore Supra antenna was dissipated on the antenna structure itself. The amount of power dissipated in the SOL plasma is generally modest. One exception is NSTX, exploiting the high-harmonic FW heating scheme, where the core heating efficiency was reported to drop by up to 60% in adverse scenarios (lower $k_{//}$ in excited spectrum, lower magnetic field) [38].

2.4. Enhanced wall erosion and core plasma contamination

More energetic ions are also more efficient for sputtering wall elements. RF-specific impurity production during ICRH has been studied mainly in metallic machines, using as a proxy the line emission in the visible range for tungsten (W) [5, 21, 27, 39–46], molybdenum (Mo) [10, 12] and beryllium (Be) [47, 48]. In the absence of systematic measurements of V_{DC}, ASDEX Upgrade and WEST publications used the ratio of W over D line brightness as a proxy for the effective W sputtering yield in order to assess the magnitude of rectified DC potentials. Reference [27] showed first experimental correlations between local heat loads and local WI line radiation at 400.8 nm on the WEST ICRF antenna limiters: they exhibit a similar characteristic poloidal shape along the limiters, which will be detailed in section 3.3. Visible spectroscopic signals are mainly representative of the local gross erosion, while prompt redeposition may be important, especially for high-Z impurities, as verified for thermal sheaths on the JET divertor [49].

Visible spectroscopy has generally been used in conjunction with VUV spectroscopic line emission from the plasma core in order to assess the central contamination for W [5, 21, 27, 39–46, 50, 51, 53], Mo [10, 12, 27, 45, 50], but also nickel in JET [53–55], titanium or iron in EAST [45, 50], iron and copper in Tore Supra [56] and silver in WEST [27, 46]. Contamination of the plasma core has been studied extensively, as large radiation from the plasma centre can hinder the fusion performance or even the stability. Contamination is however the consequence of many combined physical processes: the gross impurity production at the wall, but also redeposition, transport to the core and MHD. When analysing the variations of core impurity concentrations, it is therefore difficult to disentangle these various processes. Transport is generally associated with modified spatial distribution of the impurities and of the plasma radiation, as assessed by bolometric and soft x-ray tomographies [51, 52]. Changes in the sources are generally correlated with changes in the visible spectroscopy signals, over specific experimental protocols discussed in section 3.5. ICRH acts on both the sources and the transport. JET discharges with mixed ICRH and NBI feature higher radiation than pure NBI-heated plasmas with the same additional power [40, 51]. This is sensitive to the antenna electric setting, and attributed to larger impurity production. However, applying ICRF waves allows flattening the tungsten profiles, which can even become hollow for central power deposition, unlike pure NBI discharges. Reference [52] invoked modified impurity transport due to flatter density profiles and more-peaked temperature profiles to interpret this change. High-performance JET discharges used ICRH extensively to avoid tungsten accumulation in the plasma core [51]. We will however focus the rest of the paper on RF-induced impurity sources.

2.5. RF-induced local plasma convection

The RF-induced SOL biasing is generally highly spatially inhomogeneous. Due to the large parallel DC conductivity of the plasma, the DC electric field ∇V_{DC} is dominantly transverse to the confinement magnetic field and likely generates $\mathbf{E} \times \mathbf{B}$ flows. On LAPD, this flow has been measured using Mach probes and correlated experimentally to ∇V_{DC} [14]. In Alcator C-mod, a gas puff imaging (GPI) diagnostic mapped the convection of density fluctuations in 2D and attributed the flow to electric drifts to estimate V_{DC} profiles [12, 17–19]. GPI recorded poloidal velocities in the range of several km s^{-1}, strongly sheared radially, while turbulent radial velocities in the SOL are typically 10–100 m s^{-1} with rather flat radial profiles. On top of other SOL transport processes (turbulence, parallel losses), the RF-induced $\mathbf{E} \times \mathbf{B}$ convection redistributes the local density in the antenna vicinity. Local density modifications were evidenced using Langmuir probes [14, 20, 28, 57–59], edge reflectometry [58, 60–62], or lithium beam emission spectroscopy [25, 62]. Although density depletion was generally reported, over-density was sometimes observed in the same experiments, depending on the probed radial/poloidal location [62, 63]. This modified the wave coupling properties on LH

waveguides magnetically connected to active ICRF antennas [20, 61, 64–67], as well as LH-related hot spots, evidenced via IR thermography [30, 63, 65].

2.6. DC currents circulation and floating potential of Langmuir probes

The above-mentioned DC current equilibration by the sheaths should be understood on average over the device: DC electric currents I_{DC} are allowed locally in conductive media (plasma, wall, ...) but should form closed circuits, thereby coupling the sheaths at different locations on the machine. As a paradigmatic example, open magnetic field lines have two extremities l and r, connected by a plasma channel with very large parallel DC conductivity. If the sheaths at the two extremities are subject to different levels of rectification, basic double Langmuir probe theory shows that all along the flux tube, V_{DC} adapts to the electrode with larger $|V_{RF}|$ and I_{DC} flows from the high-$|V_{RF}|$ boundary to the low-$|V_{RF}|$ one. Reference [3] calls this type of setup asymmetric RF sheath. If I_{DC} flows only in the parallel direction, one obtains [4]

$$\frac{e\,(V_{DC}-V_{f0})}{kT_e}=\ln\left[\frac{\exp\left(\frac{eV_{br}}{kT_e}\right)+\exp\left(\frac{eV_{bl}}{kT_e}\right)}{2}\right] \quad (5)$$

$$\frac{I_{DC}}{I_{sat}}=\tanh\left[\frac{e\,(V_{bl}-V_{br})}{2kT_e}\right]. \quad (6)$$

In the latter formula, I_{DC} is counted positively if it flows from l to r. DC current transport transverse to **B**, although weak compared to the parallel DC conductivity, may play an important role when cumulated over long parallel lengths and further complicates the electrical paths in the SOL. References [21, 68] studied DC currents collected on the side limiters of ASDEX Upgrade ICRF antennas. As expected from (6), limiter tiles of active antennas collect negative DC currents. On a passive antenna connected to an active one, the DC currents can be of either sign. Negative currents correspond to tiles with strong RF pickup, suggesting that the active antenna could induce rectification remotely. Reference [69] invoked DC currents to interpret arcs in mixed phasing JET experiments. DC currents also change the electron particle and heat fluxes onto the wall. Reference [70] invoked them to interpret left–right heat load asymmetry in Tore Supra antennas with left–right power unbalance. Reference [14] measured the DC plasma potential together with its RF oscillations using an emissive probe magnetically connected to an active antenna 65 cm away. Although V_{DC} increased significantly during ICRF, the RF oscillations were ~9 times lower in magnitude, suggesting that the rectification occurred at the antenna side of the open field lines and not near the probe. The coupled field line extremities were used explicitly as an experimental technique in LAPD: reference [9] diagnosed the sheaths at a grounded plate magnetically connected to an active ICRF antenna. The DC sheath voltage at the plate was controlled by varying the RF current applied to the radiating strap.

When a grounded wall element collects DC current, the floating potential V_f of a Langmuir probe at this location is modified. Reference [71] explains how I_{DC} acts on top of voltage rectification and can reverse the sign of V_f. Within the double probe analogy developed above, the floating potentials at the l and r extremities of a biased open field line are opposite:

$$V_{fr}=-V_{fl}=V_{bl}-V_{br}=\frac{2kT_e}{e}\,\mathrm{atanh}\left(\frac{I_{DC}}{I_{sat}}\right). \quad (7)$$

This led to re-interpreting the Langmuir probe data on the NSTX [71] and EAST divertor [59] during ICRF. On fixed divertor probes connected magnetically to ICRF antennas, V_f varied in opposite ways on the two devices during ICRF application. V_f polarity on NSTX was consistent with divertor sheaths being rectified. In EAST, it is consistent with voltage rectification on the antenna sheaths and I_{DC} flowing from the antennas to the divertor. In addition, V_f polarity changed its sign on divertor probes connecting *in front* of the EAST antennas when they were energized (see also [50]).

2.7. Other RF-induced edge processes

Figure 2 summarizes the phenomenology observed above and sketches its consistency with the expectations from RF sheath rectification. These physical mechanisms are qualitatively independent of the wave absorption mechanisms at the plasma centre. They are therefore expected for all ICRF heating scenarios. LAPD measured all the phenomena, except DC currents, on similar plasmas [14]. On top of this phenomenology, other RF-induced edge processes might co-exist locally. References [34, 72] evidenced heat loads on Tore Supra ICRF antenna limiters due to fast ion losses from the plasma core. Resonant wave modes [73], wave-filament bound states [74], RF power absorption at the peripheral LH resonance [75] and ponderomotive forces [76] have been proposed in the literature, the latter especially in the vicinity of ICRF antennas. These additional processes likely exist but have not been clearly evidenced in experiments. Consequently they will not be further discussed below.

3. 3D spatial structure of RF-induced SOL modifications

3.1. Parallel structure of 'near-field' effects

RF-induced SOL modifications have been widely observed on the active ICRF wave launchers themselves and on magnetically connected objects: nearby limiters, LH waveguides, divertors.... Figure 3 visualizes, in the visible range, field-aligned bright filaments passing in front of an active NSTX antenna and reaching the upper and lower divertors [37]. In the ASDEX Upgrade, energizing an ICRF antenna influenced the W production as well as the RF and DC currents on the limiters of a magnetically connected passive antenna [21, 68]. In JET, the footprint of an active four-strap (A2) antenna on a nearby outboard limiter moved vertically over a scan of the edge safety factor (q_{95}) on the images of a Be I filtered camera [47], except the slow mode just below the LH resonant density [75]. Although a direct excitation of sheath RF oscillations by RF waves propagating to the remote objects cannot be fully excluded, this long parallel extension is more likely

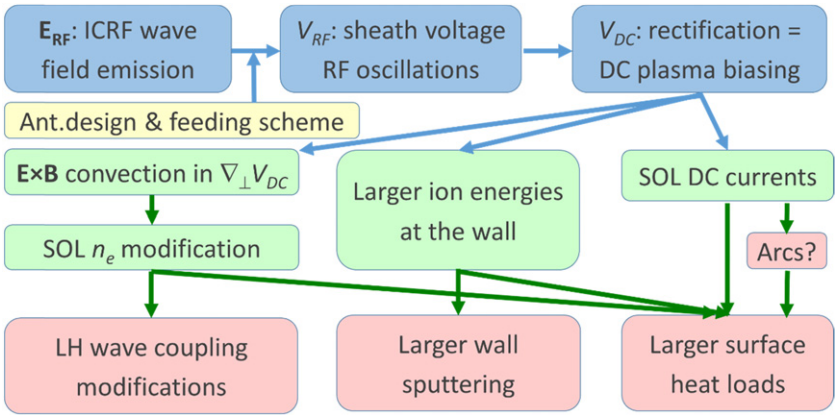

Figure 2. Sketch of ICRF-induced SOL modifications due to sheath rectification and its consequences. Blue boxes: main steps of plasma self-biasing. Green boxes: main effects of localized DC bias on SOL plasma (not specific to RF rectification). Red boxes: main operational consequences of SOL modifications, including PWI. The link between $\mathbf{E}_{RF}$ patterns and spatial structure of V_{RF}, via antenna design and feeding scheme (yellow box), is addressed in section 5 of this contribution.

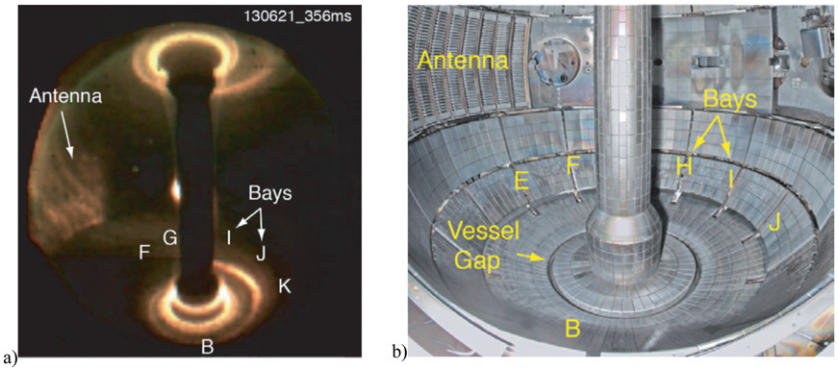

Figure 3. (*a*) Visible light image of NSTX main chamber during ICRF application in shot 130621. The plasma conditions are toroidal field 0.55 T, NBI power 2 MW. 12-strap antenna operated at 30 MHz, delivering 1.8 MW with toroidal phasing −90° between adjacent straps (main k_{ϕ} in radiated spectrum 8 m^{-1}). (*b*) Image of NSTX vessel during maintenance, showing position of the antenna, tiles, vessel gap and toroidal bay locations. View rotated 30° toroidally relative to (*a*). [] Reproduced from [37].

related to the large parallel DC conductivity of the plasma in comparison with the more modest transverse transport of DC current. In any case the launched ICRF waves are not supposed to propagate strictly parallel to **B**. Probe, reflectometry and Li beam spectroscopy diagnostics, mentioned above, measured the SOL properties several metres away toroidally from the active antennas. Parallel propagation was extensively exploited to produce 2D (radial–poloidal) mappings from these diagnostics by combining radially resolved measurements over steps of q_{95} [20, 25, 28, 58, 62, 63]. Reference [14] combined 2D probe movements over repetitive LAPD discharges. Implicitly assumed is that the measurements along the diagnostic lines of sight are representative of the SOL on the antennas. Although the SOL is modified at long toroidal distances, little is known of its parallel variation. ICRF likely affects the EAST divertor probes even if an obstacle is interposed between the antenna and the diagnostic [59], a situation described as 'blocked open field lines' in reference [13]. Most diagnostics probe magnetic field lines connected to the *lateral sides* of the antennas. More intense effects may arise in the *private SOL* created by the two antenna side limiters, as antenna reflectometry suggests for AUG [58].

3.2. *'Near-field' effects: radial structure*

2D mappings using probes, IR images of WEST and GPI data of Alcator C-mod feature strong spatial inhomogeneity transverse to **B**. ICRF-induced LH wave coupling modifications were sometimes opposite for different LHCD waveguides depending on how they connected magnetically to the active ICRF antennas [63]. In the radial direction, local maxima of V_{DC} were observed near the leading edge of the antenna limiters, with a typical extension of a few centimetres on both sides, including field lines not connected to the antenna [10, 17, 19]. Figure 4 shows the floating potential V_f recorded by a popup Langmuir probe embedded on a WEST outboard limiter over its radial stroke [27]. The probe is magnetically connected to ICRF antenna Q2. When antenna Q2 is passive, V_f is slightly negative and exhibits a smooth monotonic radial profile. When Q2 is active, a peak of positive V_f appears in the profile. Its radial shape is reproducible on the inward and outward movements of the probe. Antenna Q2 is mobile radially, and its radial position was changed from pulse to pulse. The radial location of the peak shifted radially, consistentwith this position. The bright filaments in NSTX extend radially up to

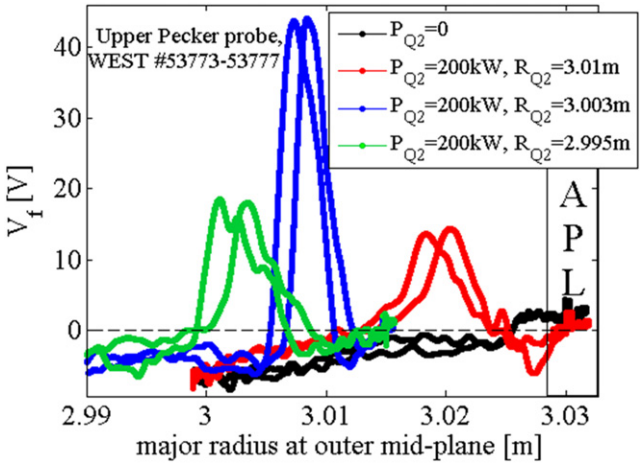

Figure 4. Floating potential of a popup Langmuir probe embedded in the WEST outboard antenna protection limiter (APL) versus radial probe location mapped to the outer mid-plane. Four probe reciprocations are represented, for several radial positions of the moveable ICRF antenna Q2. The radial location for the leading edge of the antenna limiters is indicated in the box. The inward and outward probe movements are left separate. Reproduced from [27]. CC BY 4.0.

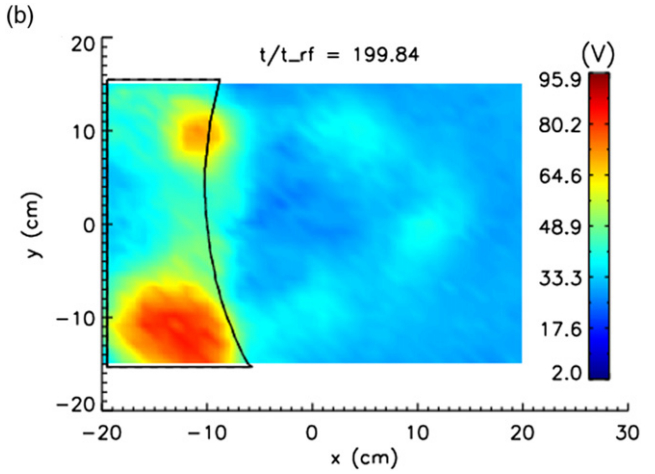

Figure 5. 2D (radial, azimuthal) map of V_{DC} recorded by a mobile emissive probe during ICRF on LAPD. The main plasma is to the right of the figure, while the antenna is on the left. The probe was located at longitudinal position $z = 65$ cm, while the active ICRF antenna was at $z = 0$. The probe moved in 2D between repetitive plasma pulses. He plasma, $B_t = 0.1$ T, $n_e = 10^{17}$–10^{18} m^{-3}, $T_e =$ 2–7 eV, $T_i \sim 1$ eV, single strap antenna in metallic box operated at 2.38 MHz, 150 kW. The black curves show the limits of the antenna box. Reprinted figure with permission from [14], Copyright (2017) by the American Physical Society.

the separatrix [37]. Reference [19] investigated the parametric dependence of the peak radial extent. This width might reveal a transverse transport mechanism, possibly enabling the DC bias to go around an obstacle, also coupling the *private SOL* between antenna limiters to the *free SOL* around it. A limited radial extent explains why the ICRF coupling resistance remains constant as the RF power increases in JET, despite the greater RF-induced density depletion [25]. This might also explain why, in JET [77] and Alcator C-mod [78, 79], nitrogen (N_2) injected near the RF-induced convective cells penetrates the core plasma in a similar way as N_2 puffed far away toroidally from the active antennas.

3.3. 'Near-field' effects: poloidal structure

In the poloidal direction, the strongest RF-induced interaction does not necessarily occur at the antenna mid-plane, even if it is radially closer to the separatrix. Instead, local maxima of the heat loads or the effective sputtering yield often develop near the antenna box corners. This multi-hump poloidal structure was observed in many devices using many techniques (Langmuir probes, emissive probes, RFA, GPI), over a large variety of antenna types [14, 16, 17, 21, 27, 28, 35, 47, 50, 58, 63]. Figure 5 maps, in 2D transverse to **B** the DC potential, V_{DC} recorded by a mobile emissive probe on LAPD [14]. In the absence of ICRF, V_{DC} remains below 10 V. During ICRF application, the image shows two peaks located near the top and bottom of the antenna box, with V_{DC} maxima exceeding 90 V. The JET ITER-like antenna (ILA) is organized as two strap arrays stacked on top of each other that can be operated independently. References [48, 62] showed that the poloidal distribution of 'near-field' effects around the ILA depends on whether its lower or upper part is energized, suggesting a strong link with RF currents flowing on the antenna structure.

3.4. Evidence of 'far-field' sheath effects

Far less documented than the above 'near-field' effects are RF-induced SOL modifications in regions never connected magnetically to the active antennas. In Alcator C-mod, DC SOL biasing was observed in the shadow of an outboard limiter, on unconnected field lines. The plasma potential enhancement there was correlated with the magnitude of local RF electric fields with FW polarization [13]. In addition, both FW fields and measured V_{DC} were modulated by sawteeth, suggesting a link with modulated single-pass absorption (SPA). V_{DC} was therefore ascribed to 'far-field' sheath excitation. Impurity production associated with 'far-field' effects is also suspected in EAST [50]. Mo is found mainly in one inner wall sector facing the EAST four-strap I-port antenna. Core Mo contamination is observed mainly when this specific antenna is energized. Figure 6 shows that, unlike other spectral lines, the Mo^{31+} line brightness from the plasma core increases as the phasing $\delta\varphi$ between adjacent straps (see figure 1) decreases and the power spectrum emitted by the I-port antenna moves to low-$k_{//}$,. This is ascribed to lower SPA. Fe in Tore Supra and Ni in JET are elements of the metallic alloys used for the main chamber wall radially far from the plasma. References [53–56] documented ICRF-specific plasma contamination by these elements: for given plasma conditions, their concentration in the plasma edge is larger when using ICRH than other heating methods. The Ni concentration in JET is fairly independent of the divertor strike point position, further suggesting a production in the main chamber. When ICRH is present, Fe and Ni densities are sensitive to the minority concentration, both in standard minority and in three-ion heating schemes. In this latter case, Ni contamination is minimized in conditions of good wave absorption. The Ni densities also

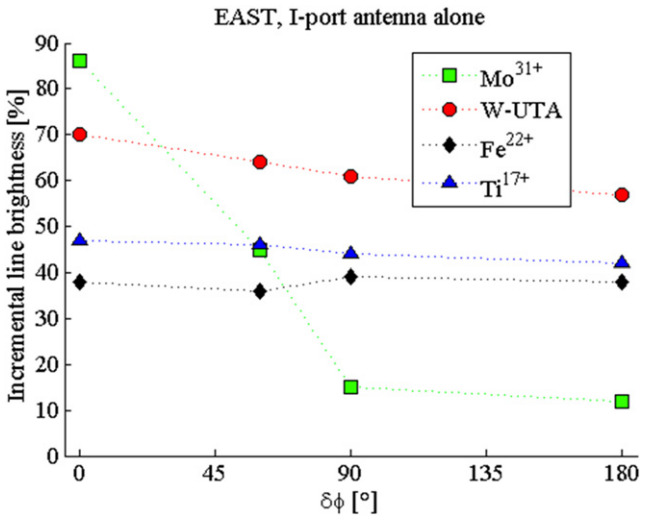

Figure 6. Increment during ICRH of normalized line brightnesses for several metallic ions in the VUV range recorded in the EAST tokamak. Mo^{31+}(127.868 Å); W-UTA(40–70 Å); Fe^{22+} (132.91 Å); Ti^{17+}(144.759 Å). The line brightness was normalized to the integrated density along the central line of sight of interferometry. The increments are the difference between during the ICRH pulse and before ICRH. The increments were subsequently normalized to the maximum increase over the list of pulses analysed, and expressed in percent. Measurements are plotted versus the phase difference between the RF currents in adjacent straps of the I-port four-strap ICRF antenna in EAST, in pulses where this antenna was energized alone. Reproduced from [50].

depend on the antenna phasings: they increase as the main $k_{//}$ in the launched spectra decreases, correlatively with lower SPA. The underlying physical mechanism is not fully identified. Candidates are fast ion losses and 'far-field' RF sheaths. The detailed geometry of 'far-field' effects is largely unknown. On top of antenna properties, it is likely sensitive to the plasma scenario, governing the propagation and core damping of the ICRF waves.

3.5. Contributions to core impurity contamination

Also scarcely addressed is the contribution of each object to the central impurity contamination. Section 2.4 explained that this is a difficult task requiring specific experimental protocols. In JET no RF-specific W-source could so far be localized directly [40]. Candidate locations could at best be 'guessed' indirectly from the SOL field lines subject to RF-induced density modifications [62]. The exercise is easier with EAST than with other devices: each region in this tokamak is characterized by a specific material that can be monitored by a specific VUV spectroscopic line [50]. In the discharges studied in figure 6, Mo is mainly found on the inner wall of the machine, W on the upper divertor, Fe on the Faraday screens, while a test Ti plate was intentionally bolted on a limiter connected magnetically to the B-port antenna. As figure 6 shows, contamination by different species can exhibit very different parametric behaviours; reference [50] evidenced physical processes specific to each region in the machine. Parametric dependencies in EAST [50] and JET [40] indicate that the W production near the divertor strike points is *not* dominated by RF effects, despite disturbed floating potentials in the EAST divertor Langmuir probes far from the strike points. Although a useful means to evidence RF-induced PWI, the Ni content in JET contributes only a small percentage of the radiated power [54]. In WEST, silver (Ag) is mainly found as a coating material for the antenna elements. Ag radiation in the VUV range is detected specifically during ICRH. This is attributed to a sputtering of the Faraday screens exposed to the plasma, but is not considered as the main radiator in WEST plasmas. In AUG, the W-coated antenna limiters were identified as major contributors to core contamination, with or without ICRH [80]. Replacing W with B in the limiters of two-strap antennas reduced the measured core W density [39, 41]. The estimated reduction in the incremental W content during ICRH could reach 70% [39]. A significant contribution from W tiles in LH antenna limiters is also reported in EAST, even in ohmic regimes, from USN/LSN comparisons of the VUV spectroscopic measurement [50]. Reference [10] characterized Mo sources Γ_{Mo}, core Mo content N_{Mo} and their dependences on the Alcator C-Mod operational regimes. The penetration of Mo into the core plasma under different conditions was analysed using the concept of penetration factor, $PF = N_{Mo}/\Gamma_{Mo}$ (s). This concept however mixes source and transport effects. The probed locations included the divertor, the inner wall and the ICRF antenna limiters. In general, the inner wall Mo source was large but was found to be relatively uncorrelated with core Mo content in diverted plasmas. The outer divertor source likely dominates core Mo content during diverted ohmic discharges. With the addition of ICRF heating, the antenna protection tile sources, even though generally smaller than that of the outer divertor, likely become an important contributor. Localized boronizations allowed for the identification of small-size sources of Mo near the divertor entrance in magnetic field lines connected to the antennas and which contributed to core contamination [81].

4. Link with the geometry of RF currents flowing on the antenna structure

Linking the spatial distribution of V_{RF} and the pattern of RF current flows on the antenna structure or that of emitted RF electric fields in realistic geometry is a topic of active research. The exercise only makes sense for 'near-field' effects that depend on a limited number of antenna and plasma parameters. The challenge is to find an antenna electric setup efficient at launching the FW while minimizing the SOL disturbance. In the antenna design phase, the main task is optimising the shapes of the main antenna components (straps, boxes, Faraday screens, septa, see figure 1). The optimisation followed several guidelines, with variable success. Once the antenna electric design is frozen, the remaining operational degrees of freedom are the ways to energize the strap array, i.e. the power sharing between the feeding transmission lines and phase difference between feeding voltages. Below we will write the phases of the successive straps in the array in radians between square brackets [...].

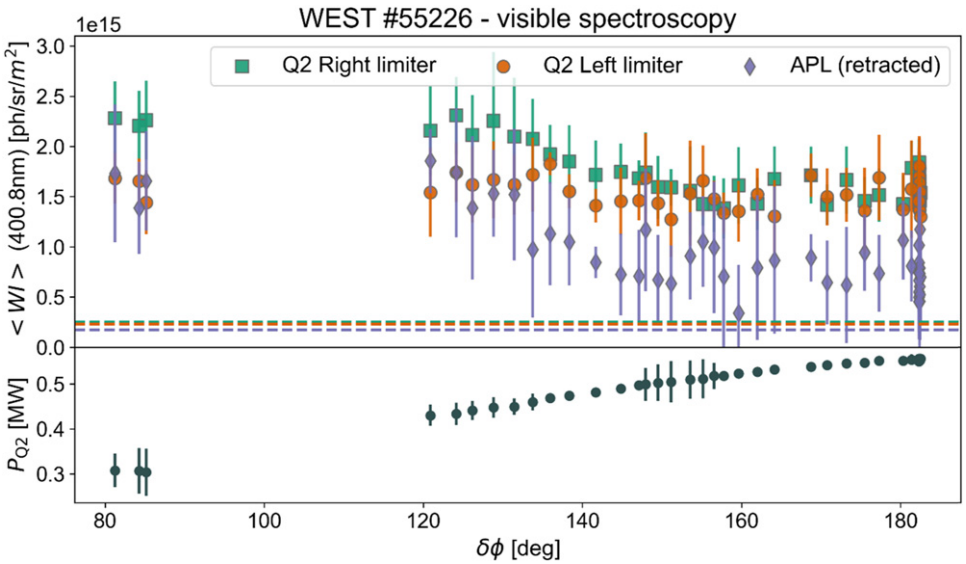

Figure 7. Upper panel: WI line brightness (wavelength 400.8 nm) averaged over all lines of sights in the left- and right-side limiters of the active WEST ICRF antenna Q2 (as seen from plasma side), as well as the outboard limiter (APL) connected to the Q2 antenna and retracted 2 cm behind it. Points plot the line brightness versus strap toroidal phasing during ICRF, and vertical lines represent the rms fluctuation level over 50 ms-wide sliding time windows. Dashed lines: value before ICRF. Lower panel: coupled ICRF power versus phase. Reproduced from [84].

4.1. Scaling of 'near-field' effects with RF voltages on feeding transmission lines

For a given plasma and antenna electrical setting, LAPD checked the linearity of V_{DC} in connected field lines with the amplitude of the RF current feeding the strap, with some offset due to the thermal sheath [82]. Consistent with this check, at a fixed feeding scheme and fixed background plasma, V_{DC} in connected field lines in Alcator C-mod generally scales as ${P_{local}}^{1/2}$, where P_{local} is the ICRF power delivered by the connected antenna [11, 12, 17, 19]. The amplitude V_{ant} of RF voltages in the transmission lines (see figure 1) also influence the RF-induced heat loads. Empirical scaling laws were proposed in [29, 31, 34, 35]: at fixed antenna phasing, heat fluxes scale as V_{ant} (proportional to V_{DC}) or faster. This latter parametric dependence is attributed to an RF-induced local density increase at the hot spot locations, while scaling laws rely on unperturbed SOL densities measured far from the antenna. The RF-induced density change is expected to depend on ∇V_{DC}, whose magnitude increases with larger V_{ant} (see e.g. [14, 25]). Linear RF power coupling to the core plasma scales as ${V_{ant}}^2$, while RF sheath power dissipation scales differently and is expected to dominate the antenna loading at low V_{ant}. This led reference [83] to propose low-power RF measurements as a way to diagnose 'near-field' RF sheath losses.

4.2. Two-strap antennas: effect of strap phasing and power sharing between transmission lines

For two-strap arrays, the wave–SOL interaction is minimized with balanced strap power and $[0\pi]$ phasing. In WEST, the phasing $\delta\varphi$ between left and right RF voltages on the matching capacitors (see figure 1) is controlled in real time [84]. Figure 7 plots the WI line brightness in two antenna side limiters and in a nearby passive limiter over a dynamic $\delta\varphi$ scan. Although dipole phasing is a local minimum, the WI line brightness is significantly larger than in an ohmic regime, and at similar power in a passive antenna. As $\delta\varphi$ decreases from 180° to 80°, the brightness in the right limiter increased by a factor 1.5, although the coupled power P_{ICRF} decreased by a factor of 2. If we apply a factor $\sqrt{P_{ICRF}}$ to compensate for the lower RF power, the normalized brightness increases by ∼1.8. Over the same phase scan, $\Delta P_{rad}/P_{ICRF}$ evolves from 45% (comparable to LH-heated discharges) to 80%. In JET discharges at similar antenna voltage and density at the antenna, the heat loads were 2.5 higher with −90° phasing than with 180° phasing [31]. An overshoot of the heat loads was recorded at the beginning of the ICRF pulses, when the RF voltages were not properly balanced between the straps.In Tore Supra two-strap arrays phased $[0\pi]$, when the power was intentionally unbalanced, the heat loads increased in the antenna limiter near the strap with larger voltage, and decreased in the opposite limiter [36]. A similar observation was made for the RF current in the limiters of the AUG two-strap antenna [85]. The toroidal width of the antenna limiters [39] and the type of Faraday screen [35, 36] also influence the magnitude of RF sheath effects.

4.3. Four-strap antennas with balanced powers: effect of strap phasing

In the JET four-strap (A2) antennas with power balanced between the straps, core plasma performance was degraded with $[00\pi\pi]$ phasing, as compared with $[0\pi0\pi]$ or $[0\pi\pi0]$ phasing at similar coupled ICRF power, despite the lower RF voltages in the feeding transmission lines [86]. Switching from $[0\pi0\pi]$ to current drive strap phasing enhanced the heat loads in the JET A2 antennas [29, 31], core W contamination [40]

and the RF-induced SOL density modifications [25]. ASDEX Upgrade emulated a balanced four-strap array by pairing two nearby two-strap antennas phased [0π] at the same frequency [39, 87, 88]. The phasing between the antennas was real-time controlled. This affected the local WI line brightness at the antenna limiters, suggesting that the whole array behaves as a single wave launcher below a minimal inter-antenna toroidal distance. However, the brightness variations with phase were location dependant, and sometimes opposite on the two antennas, so that the net effect on core W content and plasma performance is less pronounced than the local variations. Reference [89] reported first attempts at pairing two-strap and three-strap AUG antennas.

4.4. RF sheaths at antenna box corners

SOL modifications often exhibit local maxima in tilted magnetic field lines connecting near antenna box corners, i.e. that do not pass in front of all the radiating straps in the array. To act on the RF sheaths at these specific locations, the Faraday screen of one AUG two-strap antenna was partially closed using metallic corner covers. References [21, 87] compared W sputtering yields with and without a cover with balanced power and [0π] phasing: the local maxima were still present at the same location, suggesting that the excitation of sheath oscillations cannot be reduced to a matter of the line-integrated RF electric field.

4.5. Field-aligned antennas

While current straps are ordinarily purely poloidal, reducing the radiated parallel RF electric field integrated along tilted magnetic field lines, especially for four straps phased [0000], led to aligning the whole antenna structure with the oblique confinement magnetic field for a standard value of q_{95}. In Alcator C-mod, as figure 8 shows, the power radiated by the plasma was 20%–30% lower for a four-strap field-aligned-antenna (FA) heated discharge than a similar plasma heated with the toroidally aligned (TA) antenna phased [0π0π] [12]. Correlatively, the MoI line brightness decreased on lines of sight both near the FA antenna and far from it, and the MoXXXI line radiation was reduced in the core. However, the GPI and emissive probes observed nearly identical V_{DC} near an antenna box corner for FA and TA antennas when operated in [0$\pi\pi$0] phasing. Moreover, the highest V_{DC} were observed using [0000] phasing with the FA antenna. Thus, while impurity sources and contamination are indeed reduced with the FA antenna configuration, the reasons for this improvement remain to be understood.

4.6. Insulating materials

Reference [90] explains how insulating materials could help to locally mitigate the RF sheath rectification: as its RF impedance is put in series with the sheath RF impedance, a thin dielectric layer can take up part of the oscillating voltage induced by RF waves at the walls. As dielectrics behave capacitively, this leads to V_{RF} reduction at the sheath, provided that the sheath is capacitive too. This arises mainly at low density such that the ion plasma frequency is smaller

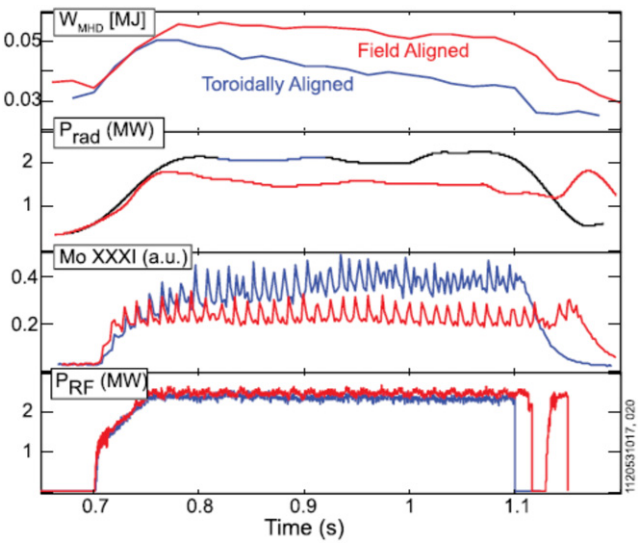

Figure 8. Time traces of plasma energy content, power radiated by the plasma, MoXXI line brightness, and ICRF power coupled by TA antenna (blue) and FA (red) antenna phased [0π0π] in Alcator C-mod. Reprinted from [12], with the permission of AIP Publishing.

than the RF wave frequency [3, 7]. As the dielectric layer becomes thicker, all RF currents can be suppressed locally. Insulating materials also locally block the DC currents. Yet, this does not necessarily mean that the plasma DC potential is reduced: insulating wall elements are floating and no longer grounded, and V_{DC} is determined by more global I_{DC} balance over the device. In the Phaedrus-T tokamak, triple probe measurements in the edge region evidenced enhanced plasma potentials near the bottom of a two-strap antenna equipped with a slotted-side Faraday screen, without antenna limiters [16, 91, 92]. Boron nitride (BN) insulating plates were subsequently installed at the sides of the FS. They suppressed the potentials and reduced the metallic impurity content of the core plasma. Following these promising results, bulk BN tiles were installed on Alcator C-mod antenna limiters [11, 81, 93]. The outcome was not fully satisfactory. In the first experiments, electric arcs occurred at the BN–metal connections exposed to the plasma. Moving the interfaces farther from the plasma suppressed the arcs. Despite impurity source removal in the antenna limiters, large DC potentials were still recorded in connected field lines. RF-specific Mo sources were detected at other locations in the main chamber magnetically connected to active ICRF launchers. In addition, reference [94] suggests that bulk BN could act as a hydrogen reservoir and complicate the control of the H minority fraction. Later, LAPD operated a single strap inside a box with bulk ceramic side walls [82]. The measured V_{DC} outside the box nearly vanished, suggesting a key role of the box currents in RF sheath generation.

4.7. Active reduction/suppression of induced RF currents

A related mitigation route is active reduction/suppression of RF currents induced at key locations. A three-strap array phased [0π0] [5, 42, 43] and four-strap arrays phased [0$\pi\pi$0] [95] or [0π0π] [95, 96] achieved strong RF sheath reduction

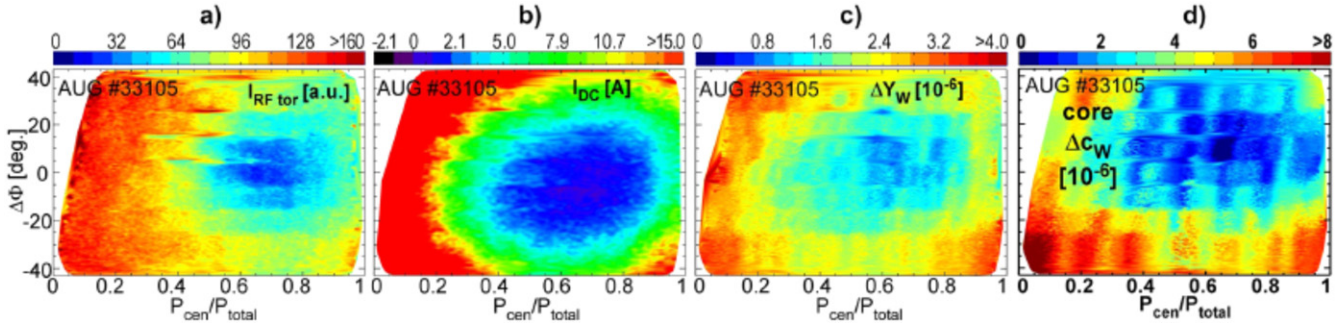

Figure 9. 2D diagrams of four quantities versus inter-strap power balance P_{cen}/P_{total} and phase deviation from dipole $\Delta\Phi$ in AUG three-strap antenna. (*a*)–(*c*) Local measurements at a single antenna limiter tile (vertical position $z \approx 0.2$ m, left limiter as seen from the plasma) of the collected RF current amplitude $I_{rf\ tor}$ (*a*), DC current circulation I_{DC} (*b*) and increment of the W effective sputtering yield ΔY_W (*c*) and (*d*) increment of W content in plasma at $T_e \approx 1.5$ keV from quasi-continuum VUV emission. Plasma parameters in discharge #33105: ELM mitigated H-mode plasma at high density, with $P_{ICRF} = 1$ MW ($P_{total} = 500$ kW coupled from the observed antenna) and $P_{NBI} = 5$ MW, D[H] minority heating at $f_0 = 30$ MHz and $B_t = 2.0$ T. Reference for increments in panels (*c*) and (*d*): NBI-only phase before ICRH. Reprinted from [5], Copyright (2019), with permission from Elsevier.

in the antenna side limiters by requesting more power in the inner straps. Figures 9(*c*) and (*d*) show the increment of local effective sputtering yield in the three-strap AUG antenna, as well as the incremental tungsten density in the plasma edge, versus the phasing and power sharing between the central and peripheral straps. They show a local minimum in local impurity production and contamination for $P_{cen}/P_{tot} = 0.7$. JET A2 antennas with [$0\pi0\pi$] phasing also achieved a locally minimal Be production, but with excessively unbalanced strap power [95]. Minimization comes with a less flexible $k_{//}$ spectrum (e.g. less easy current drive) and lower maximal power in the case of the JET A2 antennas. All local minima in RF sheath effects, including in two-strap arrays, correspond to lower RF currents induced on *both toroidal sides* of the antenna box, as evaluated by linear antenna codes without sheaths, and measured in AUG antenna side limiters [5]. For the AUG three-strap antenna with optimal feeding, figures 9(*a*) and (*b*) show that the RF currents collected in the limiter tile were nearly cancelled, and the DC current circulation there was also largely reduced. Antenna box currents might explain the universality of the multi-hump poloidal structure observed for 'near-field' effects over a large variety of strap electric schemes. For JET A2 antennas, the RF currents in the central septum also need to be reduced [5]. One can hardly cancel them simultaneously with those on the sides of antenna boxes.

5. Effect of local plasma on 'near-field' RF-induced SOL modifications

Sheath rectification is a plasma process likely affected by the plasma parameters. This section restricts the discussion to the role of local plasma parameters in 'near-field' sheath effects. 'Far-field' effects likely depend on more global profiles governing the wave propagation, refraction and damping in the plasma core.

5.1. Role of local plasma parameters in particle fluxes

Local plasma density and temperature determine the flux of particles hitting the wall and the charge state of light impurities. The magnitude of DC currents collected by AUG antenna limiters also increases with the plasma density [68]. This, together with the ion energies, determines the heat loads and gross erosion rate of the PFCs. At a given antenna voltage, the scaling laws for heat loads on the wave-launching structures depend on the local density at the antenna radial location [29, 31, 35]. At a given antenna voltage, the gross W production in WEST antenna limiters was larger when ICRF waves were applied in LH-heated discharges than in ICRH-only pulses [44]. This was ascribed to enhanced particle fluxes onto the antenna limiters in the presence of large LH power, as indicated by larger DI_δ line brightness recorded by visible spectroscopy and larger ion saturation current collected by Langmuir probes embedded in the LH antennas. As stressed in reference [32], the local density and temperature may vary along the ICRF antenna limiters if their poloidal shape is not conformal to magnetic surfaces. Along the WEST antenna limiters, this manifests in the poloidal profiles of DI_δ line intensity [45, 46]. RF-induced density convection further complicates this poloidal structure: references [33, 35, 36] invoked the convection to interpret up-down heat load asymmetries in Tore Supra antenna boxes that reversed upon **B**-field reversal. For all these reasons, the geometry of heat fluxes or impurity sources may be even more complex than that of rectified DC potentials. Reference [68] reported that the poloidal variation of WI line emission depends not only on the two-strap antenna electrical setup, but also on the plasma configuration.

5.2. Role of local density in DC potentials

The local plasma density may also act on the rectified plasma potentials. Upon a 20% increase of plasma density, reference [22] reported a two-fold reduction of the floating potential in a Langmuir probe connected to an active antenna,

while the antenna coupling resistance decreased by only 20%. Reference [13] observed opposite parametric variations of V_{DC}. When probing field lines connected to an active antenna, and for plasmas tenuous enough that the slow wave is propagative, a V_{DC} increase appeared above a critical local density, and then increased with density. This trend is qualitatively consistent with sheath rectification involving a slow wave propagating from the antenna. When probing field lines unmapped to an antenna, an opposite trend was found: V_{DC} decreased with local density over the explored (low) density range.

5.3. Control of local density with localized gas injection

On top of its 'natural' evolution, the local density in the antenna vicinity may be more actively controlled. Local gas injection was applied successfully to restore good LH wave coupling in ICRF-disturbed convective cells [65] and to enhance ICRF wave coupling without disturbing the plasma core in H mode [1]. Local D_2 injection also lowered the W production at the AUG antenna limiters [5, 97]. Reference [5] showed that the reduction is all the more pronounced as the gas is injected close to the antennas toroidally. In JET, references [53, 98] showed that core plasma radiation, the W concentration estimated at $r/a \sim 0.3$ and the Ni concentration in the plasma edge decreased as the amount of puffed gas increased. For a given amount, the total radiation was about 15%–20% lower when the gas was fuelled from the main chamber as opposed to divertor fuelling, correlating with the lower core densities of W and Ni observed in these cases. The exact reasons for the reduced impurity contamination with local gas puff are not fully understood. Larger ICRF coupling resistance reduces the local 'near-field' RF magnitudes for a given coupled power, thereby reducing 'near-field' RF sheath oscillations and associated enhanced sputtering. Other possible causes include local SOL plasma cooling, reduction of low-Z ion charge, local impurity dilution, reduced penetration of eroded material or modified prompt redeposition. More work is needed to sort out which mechanism prevails.

5.4. Role of intrinsic light impurities

The sputtering yield of high-Z materials by tokamak SOL plasmas is mainly governed by light impurities present in quantities of a few percent in a background of D^+. Reference [21] provides effective sputtering yield estimates for W in the presence of C, O and B impurities with several ionization states, while [11] shows similar curves for Mo with B^{3+} and Mo^{3+} ions. Although scarcely documented, the metallic impurity production might strongly change from one experimental day to another, likely due to varying light impurity content. References [21, 94] showed the benefits of boronizations, both in reducing the amount of light impurities, and in covering the plasma-facing high-Z surfaces with low-Z coatings. Both papers however stress that these benefits last only for short periods, or equivalently for low cumulative injected energy. In Alcator C-mod, with ICRF, the erosion rate of low-Z films is estimated to be 15–20 nm s^{-1}, indicating the eroding species energy is much higher than that normally found in the SOL [11]. Reference [94] also warned that thick boron layers might trap hydrogen. H might be released afterwards and raise the H minority content to such levels that the ICRF heating efficiency is degraded.

5.5. Antenna limiter erosion in light impurity seeding experiments

References [41, 97] reported larger W erosion on AUG antenna limiters in N_2-seeded discharges aimed at enhancing the divertor radiation, as compared to similar pure D_2-fuelled plasmas. Depending on the fraction of extrinsic impurities injected, the enhancement of effective sputtering yield could reach 1 order of magnitude in the limiters of a passive antenna [41]. When the antenna was active, the sputtering yield in its limiters increased by less than 50% in seeded discharges compared to plasmas with pure D_2 [97]. The impact of the seeding on core contamination results therefore form a trade-off between enhanced divertor radiation and larger sputtering yield. Reference [41] showed that while puffing more gas is beneficial to reduce core W content, larger gas amounts are necessary to reach a given purity in seeded AUG discharges than in pure D_2 plasmas. On the other hand, the peak values of V_{DC} estimated by GPI in Alcator C-mod decreased by about 30% when seeding with low-Z gases (helium, nitrogen and neon) [19]. It is speculated that higher neutral contents during seeding may substantially increase the collisionality/resistivity and affect V_{DC}.

6. Outlook for future long pulse metallic DT machines

This contribution reviewed recent experimental characterizations of RF-induced SOL modifications in various tokamaks and the LAPD linear device. Although not every aspect is fully clarified, significant progress has been achieved since the early review paper [2] in the comprehension and attenuation of undesirable wave–SOL interactions. This experience is extremely valuable. Indeed most of the dedicated diagnostics used in present-day machines (reciprocating probes, RFA, GPI, current sensors embedded in limiter tiles, …) can hardly be implemented in reactor-grade machines. Some diagnostics (e.g. IR thermography) are harder to operate in metallic environments, while other measurements (e.g. calorimetry of actively cooled PFCs) can only be interpreted after the pulses. Experimental time dedicated to ICRF might be limited. Future devices will therefore need to rely more on numerical simulation, backed by scarce measurements, to operate their heating systems. So far, modelling tools have been scarcely validated quantitatively against experiments in realistic geometry [4, 5, 6]. One can therefore attempt some extrapolation of the present results to future long pulse metallic DT machines, but also outline some remaining uncertainty in this prospect. It is of course desirable to reduce this uncertainty via experiments or modelling.

The SOL phenomenology observed in present devices is consistent with RF sheath rectification, although other

processes might co-exist locally and likely compete with rectification: resonant wave modes [73], wave-filament bound states [74], RF power absorption at the peripheral LH resonance [75] or ponderomotive forces [76], etc. RF sheath rectification is qualitatively independent of the way ICRF waves are damped in the plasma core. The present results are qualitatively similar in the D[H] minority and in the high harmonic heating schemes, corroborating this relative independance. Therefore, qualitatively similar phenomenology is expected in future DT devices that will exploit other ICRF heating scenarios. However the magnitude of the ICRF-induced SOL modifications likely depends on the details of the heating scheme. This is a source of quantitative uncertainty, but general guidelines can be followed to mitigate the RF sheath effects.

Mainly 'near-field' effects have been documented so far. 'Far-field' RF sheaths are suspected in some devices but remain largely unknown. The only robust method to reduce them is to ensure high single-pass absorption for the launched FW. A large machine size and a hot plasma core increase this wave absorption. ITER plans to use ICRH with a full nominal toroidal magnetic field (5.3 T on magnetic axis), half field (2.65 T) and third field (1.8 T) to heat successively hydrogen, helium, deuterium and finally DT plasmas [99, 100]. At least one ICRH scenario featuring good single-pass absorption is available for each field value and majority species. The only exception is H plasmas at half magnetic field. For this specific application, operating ITER at 3 T or 3.3 T is presently being explored. Avoiding the excitation of low-$k_{//}$ power spectra also improves wave absorption in the core. This also reduces the excitation of coaxial modes or wave damping in the peripheral LH resonance [75].

'Near-field' RF sheath effects appear in open magnetic flux tubes connecting near active ICRF antennas. High-Z materials should be used with care there. Other objects might be affected along these field lines. Apart from the wave launchers themselves, small-size regions far away toroidally from the antennas can also be sputtered and contribute to core plasma contamination. Although the RF-induced SOL disturbances can reach the divertor, there is no sign in present devices that sheath rectification dominates the sputtering there and enhances core contamination. In present devices, the disturbed zones extend radially a few centimetres in front of the antenna limiters. This suggests that SOL modifications could be kept far away from the separatrix by increasing the radial gap to the antennas (nominal value $\sim$15 cm in ITER), at the expense of lower ICRF coupling resistances.

Recent experiments have clarified the link between the geometry 'near-field' RF sheaths and the RF current patterns over metallic antenna surfaces. In Alcator C-mod, a field-aligned antenna successfully reduced the impurity production and contamination [12]. Yet, the reason for this improvement remains unclear. Such antennas hardly fit in a mid-plane port. Together with tilting the antenna, image current suppression on the sides of antenna boxes is a promising technique successfully tested on various antennas already. Using insulators for antenna boxes looks difficult in reactor environments, due to the ageing of ceramics under neutron fluxes. Active image current cancelation on the sides of metallic antenna boxes requires arrays of three straps at least, with constrained $k_{//}$ spectra and possibly power limitations. Calculations however show that antenna box currents could be cancelled in the ITER antenna box using [$0\pi\pi0$] phasing and with a reasonable power balance between the straps ($P_{\mathrm{central}}/P_{\mathrm{tot}}$ close to 0.5) [5]. Electromagnetic calculations also stress the need to avoid protruding elements on the antenna front face. Field-alignment can be combined with image-current reduction to limit ICRF-induced impurity production, as reference [96] proposed for the SPARC project. Other antenna approaches have been proposed for fusion reactors, e.g. travelling wave arrays (TWAs) [101]. In TWAs, only the first and last strap of the array are connected to transmission lines, so that one cannot control from outside the ratio of (complex) RF currents between adjacent straps. However, since the wave excitation is split between a large number of elements, the RF current magnitudes are reduced, which is attractive. TWAs remain however to be tested at high power in metallic environments.

The magnitude of 'near-field' RF sheath effects depends on the local plasma parameters. Large uncertainty remains both about the density value at the ITER wall and how this local density acts on the RF sheaths. For this reason, quantitative predictions of RF sheath effects remain delicate for future devices, although relative comparisons are certainly more reliable. ICRF coupling studies, e.g. in [75], have mainly used low-density profiles in the SOL to estimate lower bounds of the power that can be launched by the ITER antenna. Conversely, pessimistic estimates of the heat loads onto the wall elements surrounding the ITER antenna instead used high-density profiles, due to the larger particle fluxes [102].

Light impurities contribute to the sputtering. This stresses the need to maintain good machine conditioning over long high-power discharges. Extrinsic light species might be injected on purpose for reducing the divertor heat loads. This should not however hamper other aspects of the scenario, and the global impact of impurity seeding on plasma performance should be assessed. Wall erosion also changes with the majority species. While most present experiments have been conducted in D^+ plasmas, fusion reactors will operate with a DT fuel mix, with a small amount of He ash. Both T^+ and He^{2+} exhibit higher sputtering yields than D^+. The propagation (e.g. cut-off density) and damping properties of the FW also depend on the mass and charge of the majority species. JET researchers are presently investigating isotopic effects on RF–SOL interactions, and will also experiment with ICRF heating schemes planned for the DT phase at full-field in ITER. Local gas puffing was proposed from dedicated gas valves close to the ITER antenna in order to simultaneously improve the ICRF coupling and reduce the local impurity production [103]. This technique can be more easily used when the SOL is not opaque to neutrals. These can then penetrate relatively far away from the gas valve before becoming ionized. This needs to be assessed in the more opaque ITER SOL. With a poor fuelling efficiency, gas puffing in the ITER SOL should be easily decoupled from core plasma fuelling. Active control of the local plasma requires measuring the SOL density as close

as possible to the antenna, ideally with diagnostics embedded on the antenna.

Using ICRH in short-pulse D^+ plasmas, JET has achieved high-performance discharges with the mix of materials used for the ITER wall. The ITER ICRF antenna will be surrounded by Be PFCs in the main chamber. Although Be sputtering should not hamper core plasma contamination, it could be a concern for the long-term integrity of the wall. Reference [104] simulated Be erosion of a JET outer limiter connected to an active ICRF antenna, in order to match a two-to-three-fold increase in the absolutely calibrated Be I and Be II line emissions during ICRH. According to the calculations, the erosion would range between 0.15 and 0.25 nm s^{-1}, depending on the assumptions. Under the same operational scenario and for an ITER-like 400 s-long pulse, an erosion of 60–100 nm/pulse would be expected. Similar quantification should be repeated with SOL and antenna conditions as expected for ITER.

Due to the low melting temperature of beryllium (1250 °C), heat fluxes onto the PFCs surrounding the ITER ICRF antennas raise concern. IR thermography is more difficult in metallic environments than in past carbon machines due to low (and evolving) surface emissivity, together with spurious light reflections. Quantifying fluxes from IR surface temperatures also requires knowing the thermal properties of the antenna. Cooling down time constants, however, suggest that these properties can slowly evolve over experimental campaigns or antennas. In Tore Supra [72] and JET [29], inspection at shutdown revealed localized carbon deposits on the surface of CFC tiles or localized flaking of the boron carbide coatings. To help in IR data interpretation, it is therefore useful to develop monitoring pulses and repeat them regularly over the experimental campaigns, especially after incidents [72].

In Tore Supra, for each region of interest on the antenna front face, specific diagnostics have identified a physical mechanism causing local hot spots, together with a relevant actuator able to reduce the hot spots in real-time: total power, or local power from one specific IC or LH launcher. A similar exercise was performed with a selection of metallic lines in the plasma core, monitored in real-time by a dedicated VUV spectrometer [105]. In inertial machines, only a soft stop can be triggered in case of excessive heat loads or impurity contamination. In actively cooled machines more clever control schemes can be developed, e.g. continuing the pulse at reduced power, compatible with launcher integrity. In Tore Supra, five such schemes were implemented simultaneously for the record-length pulses with ICRH and LHCD [65, 106].

The mix of materials used for ITER might not be compatible with a fusion reactor. Several present devices have experimented with full coverage of their vacuum chamber with high-*Z* materials. High-performance operation of these devices was found difficult without boronization. This was not specific to ICRF-heated plasmas, but the regions magnetically connected to active ICRF antennas experience enhanced PWI. There is a consensus that boronizations between pulses last less than one single nominal discharge envisaged for ITER. This calls for more active R & D on alternative conditioning techniques, alternative materials or alternative ICRF antenna approaches.

Acknowledgments

This work has been carried out within the framework of the EUROfusion Consortium and has received funding from the Euratom Research and Training Programme 2014–2018 and 2019–2020 under Grant Agreement No. 633053. The views and opinions expressed herein do not necessarily reflect those of the European Commission.

ORCID iDs

L. Colas https://orcid.org/0000-0002-4573-3326
G. Urbanczyk https://orcid.org/0000-0002-4026-6802
J. Hillairet https://orcid.org/0000-0002-1073-6383
V. Bobkov https://orcid.org/0000-0002-2328-9308
C.C. Klepper https://orcid.org/0000-0001-9107-8337
C. Lau https://orcid.org/0000-0002-8576-5867
M. Ono https://orcid.org/0000-0001-9849-9417

References

[1] Jacquet P. *et al* 2016 Maximization of ICRF power by SOL density tailoring with local gas injection *Nucl. Fusion* **56** 046001
[2] Noterdaeme J.-M. and Oost G.V. 1993 The interaction between waves in the ion cyclotron range of frequencies and the plasma boundary *Plasma Phys. Control. Fusion* **35** 1481–511
[3] Myra J.R. 2021 A tutorial on radio frequency sheath physics for magnetically confined fusion devices *J. Plasma Phys.* **87** 905870504
[4] Colas L. *et al* 2017 SOL RF physics modelling in Europe, in support of ICRF experiments *EPJ Web Conf.* **157** 01001
[5] Bobkov V. *et al* 2019 Impact of ICRF on the scrape-off layer and on plasma wall interactions: from present experiments to fusion reactor *Nucl. Mater. Energy* **18** 131–40
[6] Zhang W. *et al* 2021 Recent progress in modeling ICRF-edge plasma interactions with application to ASDEX Upgrade *Nucl. Fusion* (accepted) (https://doi.org/10.1088/1741-4326/ac38c8)
[7] Chabert P. and Braithwaite N.St.J. 2011 *Physics of Radio-Frequency Plasmas* (Cambridge: Cambridge University Press)
[8] Lieberman A. and Lichtenberg A.J. 2005 *Principles of Plasma Discharges and Materials Processing* (New York: Wiley)
[9] Myra J.R., Lau C., Van Compernolle B., Vincena S. and Wright J.C. 2020 Measurement and modeling of the radio frequency sheath impedance in a large magnetized plasma *Phys. Plasmas* **27** 072506
[10] Lipschultz B., Pappas D.A., LaBombard B., Rice J.E., Smith D. and Wukitch S.J. 2001 A study of molybdenum influxes and transport in Alcator C-Mod *Nucl. Fusion* **41** 585
[11] Wukitch S.J., LaBombard B., Lin Y., Lipschultz B., Marmar E., Reinke M.L. and Whyte D.G. 2009 ICRF specific impurity sources and plasma sheaths in Alcator C-Mod *J. Nucl. Mater.* **390–391** 951–4
[12] Wukitch S.J. *et al* 2013 Characterization and performance of a field aligned ion cyclotron range of frequency antenna in Alcator C-Mod *Phys. Plasmas* **20** 056117

[13] Ochoukov R., Whyte D.G., Brunner D., D'Ippolito D.A., LaBombard B., Lipschultz B., Myra J.R., Terry J.L. and Wukitch S.J. 2014 ICRF-enhanced plasma potentials in the SOL of Alcator C-Mod *Plasma Phys. Control. Fusion* **56** 015004

[14] Martin M.J., Gekelman W., Van Compernolle B., Pribyl P. and Carter T. 2017 Experimental observation of convective cell formation due to a fast wave antenna in the large plasma device *Phys. Rev. Lett.* **119** 205002

[15] Kubič M. *et al* 2013 Measurement of sheath potential in RF-biased flux tubes using a retarding field analyzer in Tore Supra tokamak *J. Nucl. Mater.* **438** S509–12

[16] Tanaka T., Majeski R., Diebold D.A. and Hershkowitz N. 1996 RF generated voltage on the Faraday screen of an ICRF antenna and its effect on the Phaedrus-T edge plasma *Nucl. Fusion* **36** 1609

[17] Cziegler I., Terry J.L., Wukitch S.J., Garrett M.L., Lau C. and Lin Y. 2012 Ion-cyclotron range of frequencies in the scrape-off-layer: fine structure radial electric fields *Plasma Phys. Control. Fusion* **54** 105019

[18] Terry J. *et al* 2012 ICRF-induced radial electric fields in the far scrape-off-layer of Alcator C-Mod *Proc. 24th Int. Conf. Fusion Energy* (San Diego, USA, 8 – 13 October 2012) EX/P5-39 (http://naweb.iaea.org/napc/physics/FEC/FEC2012/papers/46_EXP539.pdf)

[19] Hong R., Wukitch S.J., Lin Y., Terry J.L., Cziegler I., Reinke M.L. and Tynan G.R. 2017 Characterization of SOL plasma flows and potentials in ICRF-heated plasmas in Alcator C-Mod *Plasma Phys. Control. Fusion* **59** 105008

[20] Colas L. *et al* 2007 2D mapping of ICRF-induced SOL perturbations in Tore Supra tokamak *J. Nucl. Mater.* **363–365** 555–9

[21] Bobkov V.V. *et al* 2010 Assessment of compatibility of ICRF antenna operation with full W wall in ASDEX Upgrade *Nucl. Fusion* **50** 035004

[22] Kubič M. *et al* 2011 Attenuation of ICRH-induced potentials in the SOL of Tore Supra *Proc. 38th EPS Conf. Plasma Physics* (Strasbourg, France, 27 June – 1 July 2011) (ECA) vol 35GP2.074 (http://ocs.ciemat.es/eps2011pap/pdf/P2.074.Pdf)

[23] Qin C.M. *et al* 2013 Experimental investigation of the potentials modified by radio frequency sheaths during ion cyclotron range of frequency on EAST *Plasma Phys. Control. Fusion* **55** 015004

[24] Perkins R.J. *et al* 2015 The contribution of radio-frequency rectification to field-aligned losses of high-harmonic fast wave power to the divertor in the National Spherical Torus eXperiment *Phys. Plasmas* **22** 042506

[25] Colas L. *et al* 2015 Localized scrape-off layer density modifications by ion cyclotron near fields in JET and ASDEX-Upgrade L-mode plasmas *J. Nucl. Mater.* **463** 735–8

[26] Urbanczyk G. *et al* 2017 Characterization of the mutual influence of ion cyclotron and lower hybrid range of frequencies systems on EAST *EPJ Web Conf.* **157** 03057

[27] Urbanczyk G., Fedorczak N., Gunn J., Colas L., Li J.G. and Wang K. 2021 Perspective of analogy between heat loads and impurity production in L-mode discharges with ICRH in WEST *Nucl. Mater. Energy* **26** 100925

[28] Colas L. *et al* 2014 Two-dimensional mapping of ICRF-induced scrape-off layer modifications with a retarding field analyser on ASDEX-Upgrade *AIP Conf. Proc.* **1580** 259–62

[29] Jacquet P. *et al* 2011 Heat loads on JET plasma facing components from ICRF and LH wave absorption in the SOL *Nucl. Fusion* **51** 103018

[30] Colas L. *et al* 2011 Heat loads from ICRF and LH wave absorption in the SOL: characterization on JET and implications for the ITER-like wall *AIP Conf. Proc.* **1406** 183

[31] Jacquet P. *et al* 2013 Characterisation of local ICRF heat loads on the JET ILW *J. Nucl. Mater.* **438** S379–83

[32] Campergue A.L. *et al* 2014 Characterization of local heat fluxes around ICRF antennas on JET *AIP Conf. Proc.* **1580** 263

[33] Colas L. *et al* 2003 Hot spot phenomena on Tore Supra ICRF antennas investigated by optical diagnostics *Nucl. Fusion* **43** 1–15

[34] Colas L., Vulliez K. and Basiuk V. 2009 Ion cyclotron resonant heating in Tore Supra *Fusion Sci. Technol.* **56** 1173

[35] Corre Y. *et al* 2012 Characterization of heat flux generated by ICRH heating with cantilevered bars and a slotted box Faraday screen *Nucl. Fusion* **52** 103010

[36] Colas L. *et al* 2013 RF-sheath patterns modification via novel Faraday screen and strap voltage imbalance on Tore Supra ion cyclotron antennae *J. Nucl. Mater.* **438** S330–3

[37] Perkins R.J. *et al* 2013 Fast-wave power flow along SOL field lines in NSTX and the associated power deposition profile across the SOL in front of the antenna *Nucl. Fusion* **53** 083025

[38] Hosea J. *et al* 2008 High harmonic fast wave heating efficiency enhancement and current drive at longer wavelength on the National Spherical Torus Experiment *Phys. Plasmas* **15** 056104

[39] Bobkov V. *et al* 2013 ICRF operation with improved antennas in ASDEX Upgrade with W wall *Nucl. Fusion* **53** 093018

[40] Bobkov V. *et al* 2013 ICRF specific plasma wall interactions in JET with the ITER-like wall *J. Nucl. Mater.* **438** S160–5

[41] Czarnecka A., Bobkov V., Dux R., Pütterich T. and Sertoli M. 2015 Trends of W behavior in ICRF assisted discharges in ASDEX Upgrade *J. Nucl. Mater.* **463** 601–4

[42] Bobkov V. *et al* 2016 First results with three-strap ICRF antennas in ASDEX Upgrade *Nucl. Fusion* **56** 084001

[43] Bobkov V. *et al* 2017 Making ICRF power compatible with a high-*Z* wall in ASDEX Upgrade *Plasma Phys. Control. Fusion* **59** 014022

[44] Colas L. *et al* 2020 First application of ion cyclotron resonant frequency waves on WEST plasma scenarios *AIP Conf. Proc.* **2254** 040004

[45] Urbanczyk G. *et al* 2020 ICRH coupling optimization and impurity behavior in EAST and WEST *AIP Conf. Proc.* **2254** 030012

[46] Urbanczyk G. *et al* 2021 RF wave coupling, plasma heating and characterization of induced plasma–material interactions in WEST L-mode discharges *Nucl. Fusion* **61** 086027

[47] Klepper C.C. *et al* 2013 RF sheath-enhanced beryllium sources at JET's ICRH antennas *J. Nucl. Mater.* **438** S594–8

[48] Klepper C. *et al* 2017 RF sheath-enhanced plasma surface interaction studies using beryllium optical emission spectroscopy in JET ITER-like wall *EPJ Web Conf.* **157** 03024

[49] Van Rooij G.J. *et al* 2013 Tungsten divertor erosion in all metal devices: lessons from the ITER like wall of JET *J. Nucl. Mater.* **438** S42–7

[50] Urbanczyk G. *et al* 2020 Metallic impurity content behavior during ICRH-heated L-mode discharges in EAST *Nucl. Fusion* **60** 126003

[51] Lerche E. *et al* 2016 Optimization of ICRH for core impurity control in JET-ILW *Nucl. Fusion* **56** 036022

[52] Goniche M. *et al* 2017 Ion cyclotron resonance heating for tungsten control in various JET H-mode scenarios *Plasma Phys. Control. Fusion* **59** 055001

[53] Czarnecka A. *et al* 2012 Impurity production from the ion cyclotron resonance heating antennas in JET *Plasma Phys. Control. Fusion* **54** 074013

[54] Czarnecka A. *et al* 2014 Spectroscopic investigation of heavy impurity behaviour during ICRH with the JET ITER-like wall *AIP Conf. Proc.* **1580** 227

[55] Chomiczewska A. 2020 Analysis of metallic impurities during the application of three-ion ICRH scenario at JET ILW *AIP Conf. Proc.* **2254** 050005

[56] Meyer O. *et al* 2007 Metallic impurity production during high power RF experiments on Tore Supra tokamak *Proc. 31st EPS Conf. Controlled Fusion and Plasma Physics* (Warsaw, Poland) (ECA) vol 31FP-4.155

[57] Bécoulet M., Colas L., Pécoul S., Gunn J., Ghendrih P., Bécoulet A. and Heuraux S. 2002 Edge plasma density convection during ion cyclotron resonance heating on Tore Supra *Phys. Plasmas* **9** 2619–32

[58] Zhang W. *et al* 2016 Modelling of the ICRF induced $E \times B$ convection in the scrape-off-layer of ASDEX Upgrade *Plasma Phys. Control. Fusion* **58** 095005

[59] Perkins R.J. *et al* 2019 Resolving interactions between ion-cyclotron range of frequencies heating and the scrape-off layer plasma in EAST using divertor probes *Plasma Phys. Control. Fusion* **61** 045011

[60] Hanson G.R. *et al* 1997 Measurements of edge density profile modifications during IBW on TFTR *AIP Conf. Proc.* vol 403 p 451

[61] Lau C., Lin Y., Wallace G., Wukitch S.J., Hanson G.R., Labombard B., Ochoukov R., Shiraiwa S. and Terry J. 2013 Effects of ICRF power on SOL density profiles and LH coupling during simultaneous LH and ICRF operation on Alcator C-Mod *Plasma Phys. Control. Fusion* **55** 095003

[62] Colas L. *et al* 2018 2D mappings of ICRF-induced SOL density modifications on JET Republic *45th EPS Conference on Plasma Physics* (Prague, Czech, 2 – 6 July 2018) vol 42A

[63] Colas L. *et al* 2007 Understanding the spatial structure of RF-induced SOL modifications *Plasma Phys. Control. Fusion* **49** B35–45

[64] Ekedahl A. 2003 Density convection near radiating ICRF antennas and its effect on the coupling of lower hybrid waves *AIP Conf. Proc.* **694** 259–62

[65] Ekedahl A. 2007 RF coupling and antenna heat load control for combined LHCD and ICRH in Tore Supra *AIP Conf. Proc.* **933** 237–44

[66] Kirov K.K. *et al* 2009 Effects of ICRF induced density modifications on LH wave coupling at JET *Plasma Phys. Control. Fusion* **51** 044003

[67] Kong E.H. *et al* 2012 Investigation of lower hybrid wave coupling and the related effects of ion cyclotron range of frequencies in EAST *Plasma Phys. Control. Fusion* **54** 105003

[68] Bobkov V. *et al* 2011 ICRF antenna-plasma interactions and its influence on W sputtering in ASDEX Upgrade *J. Nucl. Mater.* **415** S1005–8

[69] D'ippolito D.A. *et al* 2002 Modelling of mixed-phasing antenna–plasma interactions on JET A2 antennas *Nucl. Fusion* **42** 1357–65

[70] Jacquot J., Milanesio D., Colas L., Corre Y., Goniche M., Gunn J., Heuraux S. and Kubič M. 2014 Radio-frequency sheaths physics: experimental characterization on Tore Supra and related self-consistent modeling *Phys. Plasmas* **21** 061509

[71] Perkins R.J., Hosea J.C., Jaworski M.A., Bell R.E., Bertelli N., Kramer G.J., Roquemore L., Taylor G. and Wilson J.R. 2017 The role of rectified currents in far-field RF sheaths and in SOL losses of HHFW power on NSTX *Nucl. Mater. Energy* **12** 283–8

[72] Corre Y. *et al* 2011 Heat flux calculation and problem of flaking of boron carbide coatings on the Faraday screen of the ICRH antennas during Tore Supra high power, long pulse operation *Fusion Eng. Des.* **86** 429–41

[73] Perkins R.J., Hosea J.C., Bertelli N., Taylor G. and Wilson J.R. 2016 Resonance in fast-wave amplitude in the periphery of cylindrical plasmas and application to edge losses of wave heating power in tokamaks *Phys. Plasmas* **23** 070702

[74] Tierens W., Zhang W. and Myra J.R. 2020 Filament-assisted mode conversion in magnetized plasmas *Phys. Plasmas* **27** 010702

[75] Messiaen A., Maquet V. and Ongena J. 2021 Ion cyclotron resonance heating fast and slow wave excitation and power deposition in edge plasmas with application to ITER *Plasma Phys. Control. Fusion* **63** 045021

[76] Van Eester D. and Crombé K. 2015 A crude model to study radio frequency induced density modification close to launchers *Phys. Plasmas* **22** 122505

[77] Bobkov V. *et al* 2017 Progress in reducing ICRF-specific impurity release in ASDEX Upgrade and JET *Nucl. Mater. Energy* **12** 1194–8

[78] Reinke M. *et al* 2016 Experimental pathways to understand and avoid high-Z impurity contamination from ICRF heating in tokamaks *Proc. 58th Annual Meeting of the APS DPP* (San Jose, CA, 31 October–4 November 2016) (https://psfc.mit.edu/research/alcator/pubs/APS/APS2016/mlreinke_inv_2016.pdf)

[79] Wukitch S.J. *et al* 2017 Towards ICRF antennas compatible with high performance plasmas: characterization and mitigation of ICRF antenna–plasma edge interaction *22nd RFPPC Conf. Aix en Provence* Inv-08 (https://psfc.mit.edu/research/alcator/pubs/RF/rf2017index_files/Wuktich_inv_RF2017.pdf)

[80] Dux R. *et al* 2009 Plasma–wall interaction and plasma behaviour in the non-boronised all tungsten ASDEX Upgrade *J. Nucl. Mater.* **390–391** 858–63

[81] Wukitch S.J., Lipschultz B., Marmar E., Lin Y., Parisot A., Reinke M., Rice J. and Terry J. 2007 RF plasma edge interactions and their impact on ICRF antenna performance in Alcator C-Mod *J. Nucl. Mater.* **363–365** 491–7

[82] Van Compernolle B. *et al* 2019 Fast wave experiments on LAPD: RF sheaths, density modifications, convective cells and parasitic coupling *Proc. 23rd RFPPC Conf.* (Hefei) invited talk I2.8

[83] D'ippolito D.A. and Myra J.R. 1996 Low-power fast wave antenna loading as a radio-frequency sheath diagnostic *Phys. Plasmas* **3** 420

[84] Hillairet J. *et al* 2021 WEST actively-cooled load resilient ion cyclotron resonance heating results *Nucl. Fusion* **61** 096030

[85] Bobkov V. *et al* 2015 Progress in controlling ICRF-edge interactions in ASDEX Upgrade *AIP Conf. Proc.* **1689** 030004

[86] Lerche E. *et al* 2009 Recent experiments on alternative dipole phasing with the JET A2 ICRF antennas *AIP Conf. Proc.* **1187** 93

[87] Bobkov V. *et al* 2009 Operation of ICRF antennas in a full tungsten environment in ASDEX Upgrade *J. Nucl. Mater.* **390–391** 900–3

[88] Polozhiy K. *et al* 2011 Influence of the phase shift between antennas on W sputtering in ASDEX Upgrade ECA vol 35GP4.071 (http://ocs.ciemat.es/EPS2011PAP/pdf/P4.071.pdf)

[89] Bobkov V.V. *et al* 2020 Improved operating space of the ICRF system in ASDEX Upgrade *AIP Conf. Proc.* **2254** 040005

[90] Myra J.R., D'Ippolito D.A., Rice J.A. and Hazelton C.S. 1997 Radio-frequency sheath mitigation by insulating antenna limiters *J. Nucl. Mater.* **249** 190–8

[91] Sorensen J., Diebold D.A., Majeski R. and Hershkowitz N. 1993 Comparison of the effects of an ICRF antenna with insulating side limiters with and without a Faraday screen on the edge parameters of a tokamak plasma *Nucl. Fusion* **33** 915

[92] Sorensen J., Diebold D.A., Majeski R. and Hershkowitz N. 1996 Edge power deposition reduction in a tokamak by replacing the Faraday screen on an RF antenna with an insulator *Nucl. Fusion* **36** 173

[93] Wukitch S.J. *et al* 2004 Investigation of performance limiting phenomena in a variable phase ICRF antenna in Alcator C-Mod *Plasma Phys. Control. Fusion* **46** 1479–91

[94] Lin Y., Irby J., Lipschultz B., Marmar E., Whyte D., Wolfe S. and Wukitch S. 2007 Hydrogen control in Alcator C-Mod walls and plasmas *J. Nucl. Mater.* **363–365** 920–4
[95] Bobkov V. *25th International Conference on Plasma Surface Interaction in Controlled Fusion Devices (PSI-25)* (https://psi2022.kr/)
[96] Lin Y. *et al* 2020 Ion cyclotron range of frequency heating for SPARC *AIP Conf. Proc.* **2254** 030003
[97] Bobkov V.V. *et al* 2014 Influence of gas injection location and magnetic perturbations on ICRF antenna performance in ASDEX Upgrade *AIP Conf. Proc.* **1580** 271
[98] Lerche E. *et al* 2015 Impact of localized gas injection on ICRF coupling and SOL parameters in JET-ILW H-mode plasmas *J. Nucl. Mater.* **463** 634–9
[99] Lerche E. *et al* 2012 Optimizing ion-cyclotron resonance frequency heating for ITER: dedicated JET experiments *Plasma Phys. Control. Fusion* **54** 069601
[100] Schneider M., Artaud J.-F., Bonoli P., Kazakov Y., Lamalle P., Lerche E., Van Eester D. and Wright J. 2017 ICRF heating schemes for the ITER non-active phase *EPJ Web Conf.* **157** 03046
[101] Ragona R. *et al* 2019 Traveling wave array for DEMO with proof of principle on WEST *Fusion Eng. Des.* **146** 854–7
[102] Colas L. *et al* 2014 Self-consistent modeling of radio-frequency sheaths: comparison with Tore Supra measurements and predictability for future machines *Proc. 25th IAEA FEC Conf.* (St Petersburg: Russian Federation) TH/P6-9 (http://naweb.iaea.org/napc/physics/FEC/FEC2014/fec2014-preprints/457_THP69.pdf)
[103] Zhang W. *et al* 2019 Scrape-off layer density tailoring with local gas puffing to maximize ICRF power coupling in ITER *Nucl. Mater. Energy* **19** 364–71
[104] Klepper C.C. *et al* 2016 Estimates of RF-induced erosion at antenna-connected beryllium plasma-facing components in JET *Phys. Scr.* **T167** 014035
[105] Meyer O., Monier-Garbet P., Devynck P., Ekedahl A., Oddon P., Pégourié B. and Vartanian S. 2009 Impurity production monitoring during RF experiments in Tore Supra *J. Nucl. Mater.* **390–391** 1013–6
[106] Moreau P. *et al* 2007 RF heating optimization on Tore Supra using feedback control of infrared measurements *Fusion Eng. Des.* **82** 1030–5